Journal of Materials Chemistry A

Role of Solvation Site Segmental Dynamics on Ion Transport in Ethylene-Oxide based Side-Chain Polymer Electrolytes

Journal:	*Journal of Materials Chemistry A*
Manuscript ID	TA-ART-01-2021-000899.R1
Article Type:	Paper
Date Submitted by the Author:	11-Mar-2021
Complete List of Authors:	Bennington, Peter; The University of Chicago, Pritzker School of Molecular Engineering Sharon, Daniel; The University of Chicago, Pritzker School of Molecular Engineering Deng, Chuting; The University of Chicago, Pritzker School of Molecular Engineering Webb, Michael; Princeton University, Chemical and Biological Engineering de Pablo, Juan; Liew Family Professor of Molecular Theory and Simulation, Institute for Molecular Engineering Nealey, Paul; Institute for Molecular Engineering , University of Chicago Patel, Shrayesh; University of Chicago, Molecular Engineering

Role of Solvation Site Segmental Dynamics on Ion Transport in Ethylene-Oxide based Side-Chain Polymer Electrolytes

Authors

Peter Bennington[1], Chuting Deng[1], Daniel Sharon[1,2], Michael A. Webb[3], Juan J. de Pablo[1,2*], Paul F. Nealey[1,2*], Shrayesh N. Patel[1*]

Affiliations

[1] Pritzker School of Molecular Engineering, University of Chicago, 5640 S Ellis Ave, Chicago, IL 60637, United States

[2] Materials Science Division, Argonne National Laboratory, 9700 South Cass Avenue, Lemont, IL 60439, United States

[3] Department of Chemical and Biological Engineering, Princeton University, 41 Olden Street, Princeton, NJ 08540, United States

*depablo@uchicago.edu, nealey@uchicago.edu, shrayesh@uchicago.edu

Abstract

Ion conducting capability is often imparted to polymeric materials through short polyether side-chains, and yet the impact of this graft polymer architecture on ion solvation and conduction has not been fully explored. Here we use a combination of impedance spectroscopy, vibrational spectroscopy, and atomistic molecular dynamics (MD) to compare the conductivity, ionic interactions, and polymer dynamics in a series of graft polyether electrolytes. We find that in poly[(oligo ethylene oxide) methyl ether methacrylate] (POEM), a widely used graft polymer electrolyte, the ionic conductivity drops more than an order of magnitude as the side-chain length is decreased from nine ethylene oxide (EO) units to three. This difference in conductivity is unexplained by differences in the calorimetric glass transition temperature (T_g), which varies only slightly with side-chain length. Through vibrational spectroscopy and MD simulations we demonstrate that both linear and graft polyethers solvate Li^+ ions effectively and dissociate them from large counterions, irrespective of side-chain length. Li^+ ions do, however, show preferential solvation by EO units far from the methacrylate backbone. Similarly, EO units far from the backbone show enhanced segmental dynamics, while those near the immobile methacrylate group move substantially more slowly, as quantified by bond vector autocorrelation relaxation times. This heterogeneity in both ion solvation and local segmental relaxation explains variation in ion conductivity where material-averaged properties such as T_g and number of free ions fail to do so. Importantly, the ionic conductivity is dictated primarily by the segmental mobility of the EO units which form effective solvation sites, rather than system-wide dynamics.

MAIN TEXT

Introduction

Solid polymer electrolytes (SPEs) play a critical role in the development of high energy density electrochemical energy storage and conversion devices. In the field of lithium ion batteries, poly(ethylene oxide) (PEO) has long been the most promising candidate for use as a separator and electrolyte due to its ability to readily solvate and conduct alkali metal cations.[1] Many other materials chemistries have been considered for their potential as dry SPEs, such as polycarbonates[2–4] and polyesters,[5–7] but polyethers continue to outperform these other systems in terms of ionic conductivity and remain the most widely studied class of polymer electrolytes.

However, the semi-crystalline nature of PEO at ambient temperatures and resultingly low room temperature conductivity, as well as a low lithium cation transference number, and an inverse relationship between ion transport and mechanical properties have prevented homopolymer PEO from satisfying the full set of requirements to enable safe cycling of high energy density lithium metal batteries.

New directions in the field of ion conducting polymers focus on incorporating additional functionalities to the well-known ether-based electrolytes to improve on these mechanical and electrochemical shortcomings of PEO. Such materials include microphase-separating block copolymers, graft and bottlebrush polymers, and random copolymers or blends where secondary functional groups affect the phase behavior and electrochemical properties of the material.[8–14] The introduction of ethylene oxide (EO) segments as grafted side-chains on polymerizable macromonomers is a particularly attractive as this approach is accessible through a number of well-established synthetic techniques, including anionic polymerization,[15] atom-transfer radical polymerization (ATRP),[16] and reversible-addition-fragmentation chain transfer polymerization (RAFT).[17] This method has the added benefit of reducing or eliminating room temperature crystallization of the short polyether chains. These controlled living polymerization techniques are also amenable to random or block copolymerization, which have been used successfully to incorporate additional functionalities alongside the ion conducting EO groups, such as a mechanically stabilizing group or single-ion conducting component.[18–20] The ether oxygen motif has also been incorporated into materials that are tailored for electrode binder applications due to their dynamic self-healing capability[21,22] or coupled with polythiophene groups to create dual ion-electron conducting materials.[23,24] Further improvement upon the design of these multi-functional materials, however, requires a clearer understanding of how the polymer chain architecture and composition affects the solvation and transport of ions.

Ion transport in rubbery polymer electrolytes is generally understood to require a high degree of salt dissociation, connectivity between polymer solvation sites, and fast segmental dynamics to facilitate ion transport between solvation sites. PEO forms stable complexes with alkali metal ions such as lithium through interactions with the lone pairs on the ether oxygens. This enables high degree of ionic dissociation from large, stable anions, such as the common bis(trifluoromethanesulfonyl)imide ($TFSI^-$). The low glass transition temperature (T_g) of PEO gives rise to fast segmental dynamics when completely amorphous (above *ca.* 50°C), which has been shown to facilitate rapid ionic transport.[25,26] Low T_g alone, however, is not necessarily a good predictor of ionic conductivity. This fact was exemplified by a recent study of poly(trimethylene carbonate)-based polymer electrolytes, where it was demonstrated that the introduction of long alkyl side-chains lowered the glass transition temperature, but a concomitant increase in ionic conductivity was not observed.[27] Molecular dynamics (MD) simulations indicated that, although the material overall exhibited faster dynamics when alkyl plasticizers were present, the time between ion hopping events was significantly longer. Similarly, solvation site connectivity has been explored in various systems as an additional metric to accounts for the discrepancy between trends in T_g and ionic conductivity.[28–30] Previous studies have found that in branched polyethers, the length of polymer side-chains and the spacing between them are key parameters in determining the conductivity of the system.[31,32] MD studies have sought to provide mechanistic insight into the effects of branched architecture and side-chain structure on ion transport, though a clear connection between microscopic transport phenomena and macroscopic material performance was not established.[33] Recent work by our group has demonstrated that heterogenous ion solvation and local polymer relaxation rates in graft polymers result in qualitatively different trends in ion conductivity than in linear polymer electrolytes.[34] Greater understanding of how molecular-level transport processes are affected by the graft chain architecture, chemical composition, and side-chain length are required to optimize the design and development of these systems.

In this study, we synthesize, characterize, and computationally model a series of graft polyethers to examine the effects of polymer composition, chain architecture, and side-chain length on the ion solvation, average and local segmental dynamics, and transport properties of these electrolytes. We observe that the experimental ion conductivity varies by as much as an order of magnitude in poly[(oligo(ethylene oxide))methyl ether methacrylate] (POEM) materials of different side-chain lengths, and this effect is not well explained by differences in T_g or ionic dissociation. The same trend is observed in the simulated Li-ion diffusivity. Comparing solvation site edge density from MD simulations and T_g-corrected experimental conductivity, we see that solvation site connectivity, as defined in previous studies, only accurately predicts conductivity or MSD at intermediate temperatures (T). We find significant deviations above and below the solvation site predicted performance at high and low values of T-T_g, respectively. We demonstrate that although ions are fully dissociated in all systems, Li^+ ions show a strong preference for ether oxygens over carbonyl groups. Constraints on the available conformations of those ether oxygens giving rise to certain monomers having a much more significant role in solvation than others. We further see that individual EO segments relax at substantially different rates as a function of position along the side-chain. Those EO units furthest from the relatively immobile methacrylate backbone exhibit significantly faster relaxation rates than those near the backbone. This spatial variation in the segmental mobility is not captured by the T_g differences, but local EO segmental dynamics seems to be critical in producing the observed trends in ionic conductivity. Specifically, the dynamics of those EO segments which most frequently participate in the formation of solvation sites have far greater impact on the ionic conductivity than the overall segmental dynamics. Moreover, we find that making the backbone more flexible or increasing the fraction of high-mobility (far from the backbone) EO units at the same overall ether oxygen fraction both increase the ionic conductivity. These findings have broad implications for developing graft and multifunctional polymer electrolytes and provide clear design criteria for optimizing polymer architecture and chemistry for high ionic conductivity.

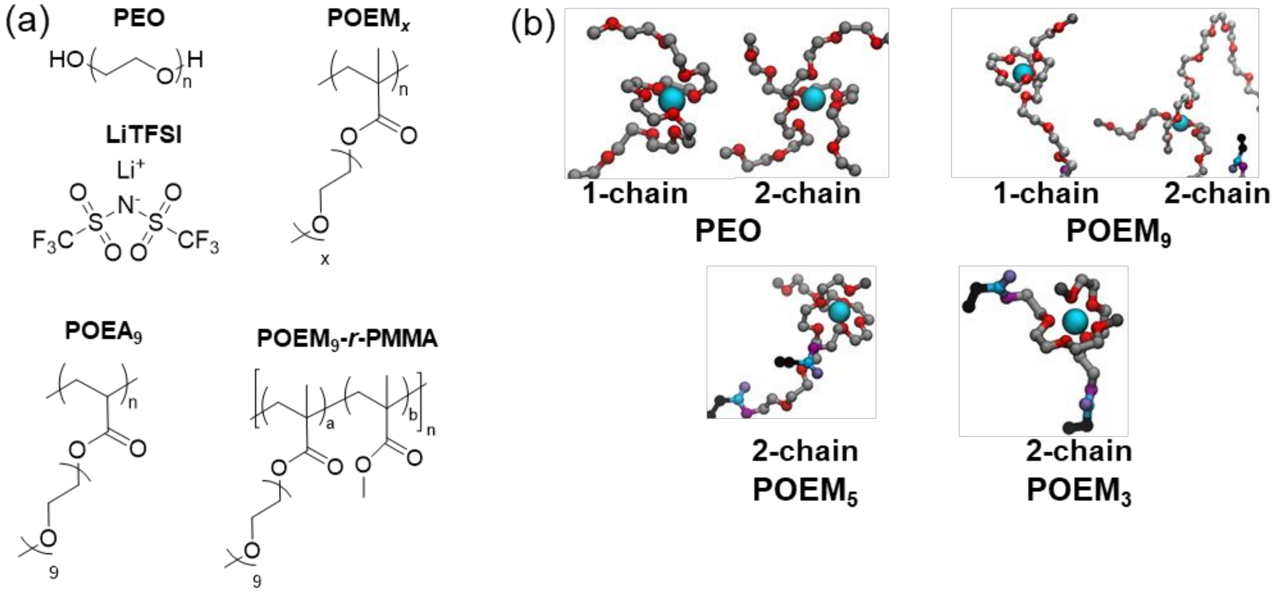

Fig. 1. (a) Chemical structure of polymers studied and LiTFSI salt; (b) Representative snapshots of united atom MD simulations showing common 1 and 2 chain solvation motifs in each system. Ether oxygen units are in red, Li^+ ions are cyan, aliphatic carbons are gray, backbone carbons are black, and methacrylate group oxygens are purple.

Results and Discussion

To explore the effects of polymer chain architecture and composition on ion conduction and solvation in EO-based polymer electrolytes, we employ a combined experimental and computational platform involving thin film electrochemical impedance spectroscopy (EIS), Raman and Fourier Transform Infrared (FTIR) spectroscopy, and molecular dynamics (MD) simulations. We investigate two classes of polyethers in this study: linear poly(ethylene oxide) (PEO), and a series of graft polymers based on short polyether side-chains grafted to an acrylate or methacrylate backbone. Side-chain polymers poly[(oligo (ethylene oxide)) methyl ether methacrylate] ($POEM_x$), poly[(oligo (ethylene oxide)) methyl ether acrylate] ($POEA_x$), and a random copolymer of POEM and poly(methyl methacrylate) (PMMA) were prepared by reversible addition fragmentation chain transfer polymerization (RAFT). The subscript *x* here refers to the number of EO repeat units in the grafted side-chain, which in this study is either 3, 5, or 9. The chemical structures of these materials are shown in Fig. 1a. The polymerization reactions were performed at 70 °C in dimethylformamide (DMF) using azobisisobutyronitrile (AIBN) as a radical initiator and 2-cyano-2-propyl dodecyltrithiocarbonate (CPDTC) as a chain transfer agent. The reaction scheme is shown in scheme S1 and S2. The number average molecular weight (M_n) and dispersity ($Đ$), as determined by gel permeation chromatography (GPC, Fig. S1), are given in Table 1. The polymer electrolyte systems are modeled by MD simulations using a united atom representation to characterize the equilibrium ion solvation structures and ion transport rates. Representative snapshots of the MD simulations are shown in Fig. 1b. Throughout the study, results from the simulations clarify and expand upon the experimental data and are used to help build a molecular level understanding of the effect of chain architecture and composition on polymer electrolyte ion conduction.

Table 1. Physical properties of materials studied

Material	M_n (g mol^{-1})	$Đ$	x_{EO}	T_g at r = 0.05 (°C)
PEO	^{1}20,000	^{1}1.10	0.333	-50
POEM$_9$	^{2}17,700	^{2}1.13	0.265	-57
POEM$_5$	^{2}33,400	^{2}1.29	0.227	-41
POEM$_3$	^{2}21,200	^{2}1.21	0.188	-31
POEA$_9$	^{2}11,800	^{2}1.08	0.273	-50
POEM$_9$-*r*-PMMA	^{2}13,500	^{2}1.17	0.172	-37

[1] As reported by the supplier

[2] As determined from GPC-MALS in THF at 50 °C using dn/dc = 0.073 mL g^{-1}

Side-chain length—not T_g—determines ionic conductivity in graft polyethers

All of the studied polymers are rendered ionically conductive by addition of lithium bis(trifluoromethanesulfonyl)imide (LiTFSI) blended at a ratio of r = [Li]/[EO] = 0.05. Note that the salt concentration is held constant with respect to the ether oxygen mole fraction of the polymer (x_{EO}), and so the mass fraction of salt in the system is not the same across different polymers. We follow the approach taken by Pesko *et al.* in defining this mole fraction.[28] Briefly, this x_{EO} quantity is the ratio of ether oxygens to the total number of atoms in the repeat unit, not including hydrogen atoms. Implicit in this choice of salt loading is the assumption that only the ether oxygen units contribute to solvation and conduction, and that the methacrylate groups constitute inactive material. The choice to hold r constant, rather than total weight fraction of salt, is common in studies of nonhomogeneous polyether electrolytes,[16,21,30] and the validity of this assumption will be discussed in greater detail in the text. After blending with LiTFSI, polymer electrolyte solutions are spin cast from either acetonitrile or a mixture of acetonitrile and toluene onto interdigitated electrodes (IDEs) that are surface-passivated with 0.8 nm SiO_2 by atomic layer deposition. These IDEs are used to perform EIS measurements on polymer films of 70 – 100 nm thickness. The resulting data is fit to an equivalent circuit model and converted to conductivity by an appropriate cell constant, as described in our previous work.[35]

The temperature-dependent ionic conductivity of linear PEO and the graft polymers $POEM_9$, $POEM_5$, and $POEM_3$, all at a salt ratio of $r = 0.05$, is shown in Fig. 2a. The ionic conductivity in $POEM_9$ is lower than that of PEO by around a factor of two at all temperatures above the PEO crystalline melting point (*ca.* 50 °C). $POEM_9$ conductivity it is still reasonably high, however, above the commonly cited benchmark of 10^{-4} S cm^{-1} at 50 °C.[36] More interestingly though, the conductivity of $POEM_x$ decreases by an order of magnitude or more as x decreases from 9 to 3. This trend in ionic conductivity as a function of side-chain length is evident from Li^+ ion mean squared displacement (MSD) observed in the simulations (see Fig. S2). At the end of the simulation time, Li^+ MSD is highest for PEO at all temperatures, and it decreases with decreasing side-chain length. Although differences in conductivity as a function of side-chain length have been observed previously in POEM and other graft polyether systems, clear mechanistic reasons for this effect have not been assigned.[31,33] Understanding why this effect arises is critical to future development of optimized polymer electrolytes based on side-chain architectures.

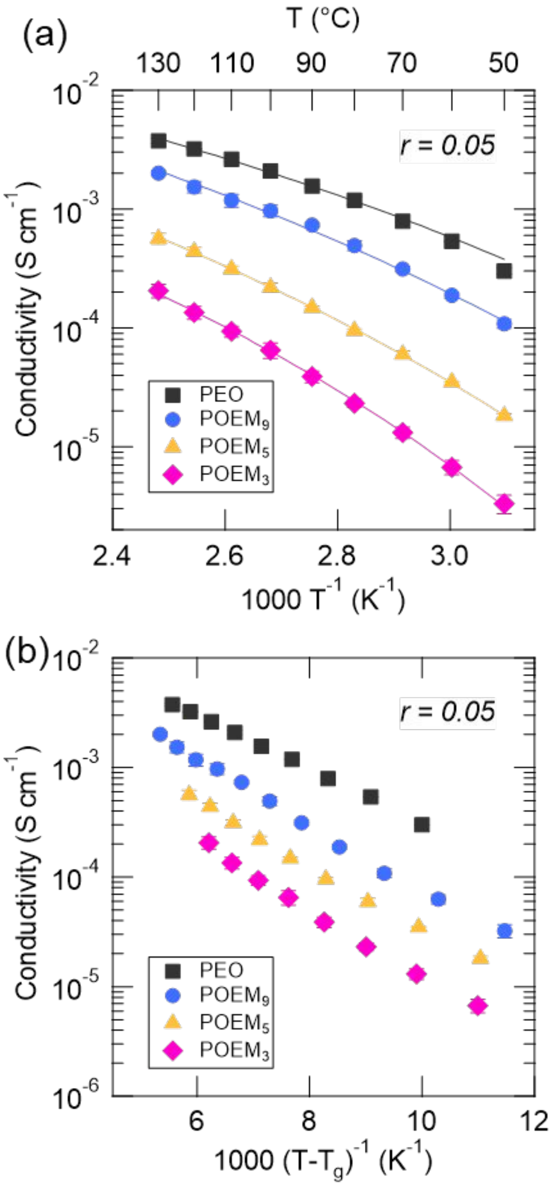

Fig. 2. (a) Experimentally determined temperature dependent ionic conductivity for $r = 0.05$ polymer electrolytes with solid lines representing the fits to the Vogel-Tamman-Fulcher (VTF) equation (*eq*. 1) and (b) experimental conductivity corrected by T_g.

Ionic conductivity is commonly understood to be tied to the segmental dynamics of the polymer host.[37] Vogel-Tammann-Fulcher (VTF) behavior of ionically conductive polymers is often cited as evidence of this connection between ionic mobility and polymer relaxation times.[25,38]

The conductivity of all four materials follow VTF behavior as a function of temperature, with fits to the VTF equation (*eq.* 1) drawn as solid lines in Fig. 2a.

$$\sigma = AT^{-0.5}\exp\left[\frac{-E_\mathrm{a}}{R(T-T_0)}\right] \qquad (1)$$

T_0 is the Vogel temperature, E_a is the pseudo-activation energy, and A is a constant prefactor.[39] As the length of grafted side-chains is known to increase the available free volume and increase segmental mobility, it is plausible that decreased segmental dynamics in POEM$_3$ chains is responsible for the low ionic conductivity.[40] T_g, as determined by differential scanning calorimetry (DSC), is a common proxy for describing the effects of segmental dynamics on conductivity. DSC thermograms for each polymer at $r = 0.05$ are shown in Fig. S3, and the values for T_g are shown in Table 1. T_g generally increases as side-chain length decreases in POEM$_x$, which would suggest generally slower segmental dynamics and therefore lower ionic conductivity in materials with short side-chains. However, by plotting conductivity as a function of 1000/(T-T_g) (Fig. 2b), it is clear that this difference in T_g is insufficient to explain the observed trends in conductivity. This common approach to correcting for differences in T_g suggests that if all corrected conductivity falls along the same line, differences in segmental dynamics explain all differences in conductivity, and T_g fully captures those differences in segmental dynamics.[41] Although linear PEO and graft POEM$_x$ seem to follow VTF behavior, side-chain length appears to have an additional impact on ionic mobility or that there are segmental dynamics influencing ionic mobility that are not captured by traditional T_g measurements.

As side-chain length effects on T_g do not provide a clear evidence that average segmental dynamics—as described by T_g— dictate the differences in ionic conductivity in graft polyethers, differences in the polymer compositions and chain architectures may instead influence the density and connectivity of solvation sites available for ion hopping. Webb and coworkers have developed a framework for quantifying the degree of solvation site connectivity based on the results of MD simulations like the ones performed here.[28–30] Briefly, a solvation site is defined at the centroid of a set of five or more ether oxygen atoms each within 3.7 Å of the centroid. These sites are shown as filled circles in Fig. 3a. Solvation sites are connected by edges if the sites are within a cutoff radius of 3 Å of each other. These edges are shown as colored lines in Fig. 3a. Note that connections between solvation sites that are farther apart than 3 Å are not shown. A more thorough explanation of the relationship between solvation site connectivity and ion transport as a function of nearest-neighbor distance can be found in previous work by Pesko *et al.*[28] Importantly, this analysis considers only ether oxygens as contributing to the formation of solvation sites. This results in an overall lower density of solvation sites and edges in POEM with lower ether oxygen mole fraction, x_{EO}, as can be seen visually in Fig. 3a. The solvation site edge density, κ, normalized by the solvation site edge density of PEO, κ_{PEO}, is shown in Fig. 3b for different POEM$_x$ materials. The value of $\kappa/\kappa_{\mathrm{PEO}}$ varies linearly with x_{EO}, as seen by the linear fit dashed line in Fig. S4. In the study of a series of linear polyethers by Pesko *et al.*, $\kappa/\kappa_{\mathrm{PEO}}$ was also found to vary linearly with x_{EO} within a given family of materials.[28] The graft architecture of the polymers, moreover, does not seem to negatively influence the density of solvation sites. Nevertheless, this monotonic decrease in solvation site connectivity as a function of decreasing side-chain length does, at least qualitatively, explain the observed trend in conductivity. Solvation site density and connectivity are also found to be independent of temperature, depending solely on the ether oxygen content and polymer chain architecture, suggesting that $\kappa/\kappa_{\mathrm{PEO}}$ represents an intrinsic material property.

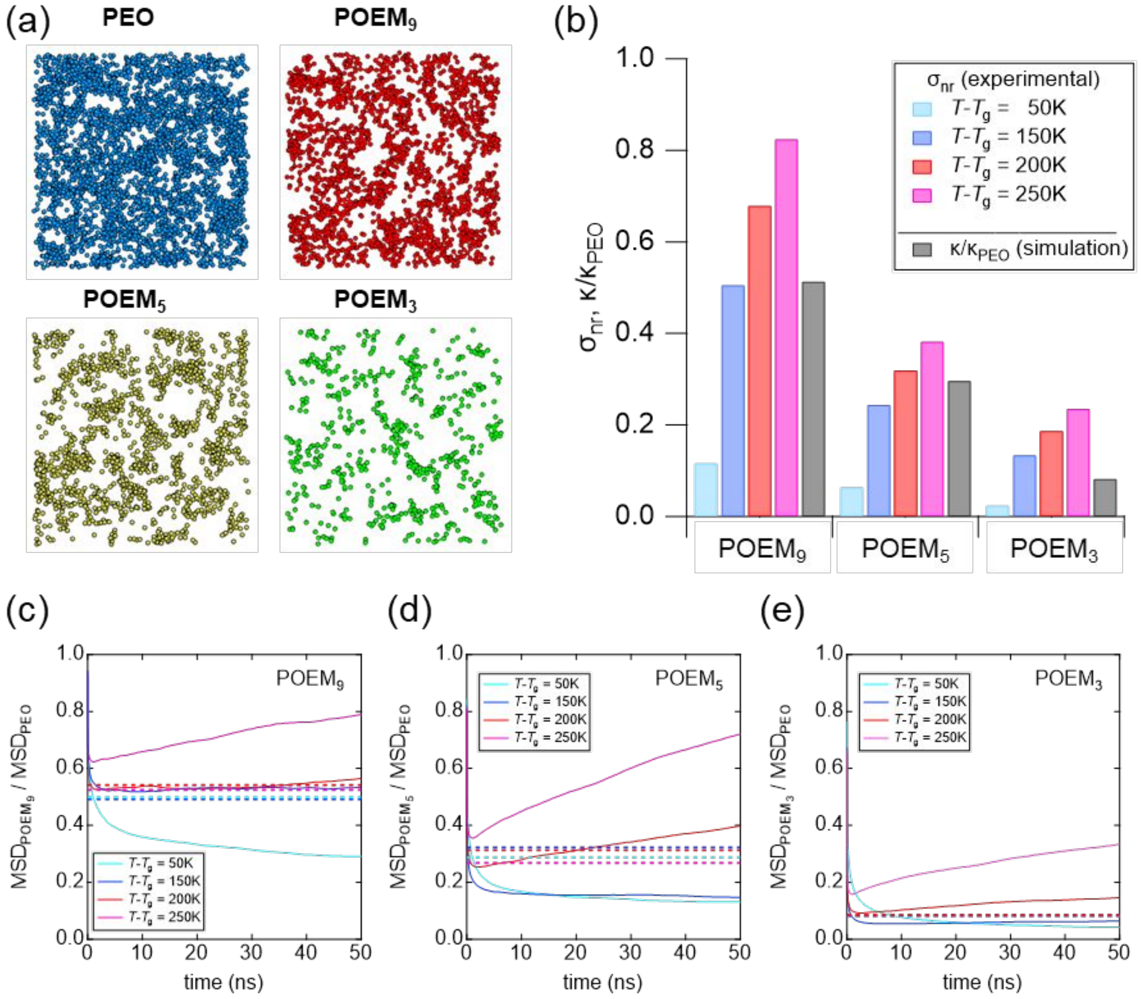

Fig. 3. (a) Visualization of solvation site network in PEO and POEM$_x$ from MD simulations; (b) Temperature averaged solvation site density ratio (gray) and normalized reduced conductivity (σ_{nr}, colors) at different fixed T-T_g for the three POEM$_x$ materials. Solvation site density and experimental conductivity are normalized to the value for PEO. Ratio of solvation site edge density (dashed lines) and Li$^+$ ion mean squared displacement (MSD, solid lines) in (c) POEM$_9$, (d) POEM$_5$, and (e) POEM$_3$ to PEO at different values of T-T_g.

To quantitatively compare the calculated solvation site edge density to the experimentally determined conductivity, we introduce a normalized, temperature-reduced conductivity, σ_{nr}, similar to the scheme used by Pesko, *et al.*[28] σ_{nr} is calculated by first determining POEM conductivity at fixed values of reduced temperature, T-T_g, using the VTF fits to the data described previously and then normalizing this value by differences in x_{EO} and conductivity of PEO, as shown in *eq. 2*.

$$\sigma_{nr} = \left(\frac{\sigma(T - T_g)}{\sigma_{PEO}(T - T_g)}\right)\left(\frac{x_{EO,PEO}}{x_{EO}}\right) \qquad (2)$$

Implicit in the use of this normalized conductivity are the assumptions that ionic solvation is similar in all materials being compared and that the effects of polymer segmental dynamics on ionic mobility are well captured by T_g and fits to *eq. 1*. If these assumptions are valid for a given set of materials and no other factors are expected to limit conductivity, σ_{nr} would represent an experimental solvation site connectivity, and it should vary with x_{EO} similarly to the solvation site connectivity calculated from MD simulations and be independent of temperature. As can be seen in Fig. 3b, σ_{nr} increases monotonically with increasing x_{EO}, suggesting that solvation site connectivity does play a critical role in determining conductivity in graft polyethers. At intermediate temperatures (T-T_g = 150 K) σ_{nr} is in excellent quantitative agreement with the simulated κ/κ_{PEO}, suggesting that this theory fully captures the important physical properties dictating ionic conductivity. σ_{nr} exhibits a strong temperature dependence for all three POEM systems, however, suggesting that this parameter is not an intrinsic to the material, as was found in previous studies.[42] At temperatures above and below T-T_g = 150 K, we see that experimental σ_{nr} deviates significantly from the simulated κ/κ_{PEO}, by as much as a factor of 5. Specifically, at low values of T-T_g, σ_{nr} is substantially lower than κ/κ_{PEO}, indicating that other factors reduce ionic conductivity that are not accounted for in this normalization scheme. Conversely, at high values of T-T_g, κ/κ_{PEO} underpredicts σ_{nr}, suggesting that there are factors increasing the conductivity of POEM relative to PEO. This difference is in contrast to the previous reports regarding linear polyethers where σ_{nr} was found to be relatively constant with temperature.[42] Note that the experimental σ_{nr} values presented here at high and low temperatures are extrapolated from fits to *eq*. 1, rather than experimentally measured, and they span a wider temperature range than was reported by Pesko *et al*. The low temperature values (T-T_g = 50K) would be below the crystallization point of PEO, making experimental measurement of the ion conductivity of amorphous PEO untenable. Nevertheless, analysis of this broad temperature range provides important insight into the temperature dependent material behavior that may be missed if only a narrow range is considered.

Fig. 3c-e shows the ratio of Li^+ ion mean squared displacement (MSD) from simulation in $POEM_9$, $POEM_5$, and $POEM_3$ to Li^+ MSD in PEO at different reduced temperatures. κ/κ_{PEO} is shown as dashed lines in each system. This value is nearly invariant with temperature, showing only slight fluctuations around an average value (the temperature averaged value is shown in Fig. 3b). Although the time scales of these simulations does not capture truly diffusive behavior, the effective diffusivity (*i.e.* the MSD rate at the end of the simulation) exhibits the same qualitative trends as was observed in the experimental system. At intermediate temperatures, the ratio of Li^+ ion MSD is close to the ratio of solvation site connectivity, whereas at high and low temperatures the MSD ratios are well above or below κ/κ_{PEO}, respectively. It is clear that this temperature dependent behavior is inherent to graft polyethers, and one or more of the critical assumptions made in using this model must be reconsidered or refined.

Chain architecture influences structure of solvation environment

Our analysis of ionic conductivity behavior thus far has relied on three critical assumptions about the solvation structure within POEM. First, we have assumed that only EO units participate in creating Li^+ ion solvation sites and facilitating ion transport, an assumption that is well supported by previous experimental and computational work involving similar systems.[30,43] Second, we have assumed a similar degree of ionic dissociation in all systems. Third, we have neglected any effect that the polymer chain architecture (*i.e.* linear *vs.* graft) may have on the solvation environment, using ether oxygen content as the only metric for comparing between materials. To validate these assumptions, we use MD simulations, Raman, and FTIR spectroscopy to fully characterize the solvation environment and ionic interactions in PEO and POEM.

We begin by confirming the assumption that ether oxygens are the only polymer functional groups interacting with Li^+ ions, and solvation sites are formed exclusively from these ether oxygen atoms. From MD simulations, we can quantify the percentage of the total oxygens within the first solvation shell of a lithium ion, here defined to be within 3.25 Å radius of the central ion, belonging to a given class of oxygen atom. Fig. 4a shows the percentage of oxygens involved in solvation that come from ether (OET), carbonyl (OKT), ester (OKE), or TFSI anion (OTFSI) groups in PEO and POEM salt blended systems. We find clear evidence that ether oxygens are the only groups involved in polymer-ion solvation for all four systems, with a very small ($< 1\%$) prevalence of ester oxygen solvation counted in the $POEM_3$ and $POEM_5$ systems. This is visually evident from the Li^+-O radial distribution function (RDF) plots shown in Fig. S5. From the RDFs it is clear that EO oxygens form nearly the entirety of the first solvation shell. These findings are consistent with previous reports of polymer electrolyte systems with multiple potential solvating groups, where lithium ions have been observed to be highly selective towards coordination by ether oxygens over ester or carbonate moieties.[30,43] We confirm this observation experimentally using FTIR. Fig. 4b shows FTIR spectra for neat and $r = 0.05$ POEM systems in the wavenumber range 1780 – 1680 cm^{-1} (full spectra are shown in Fig. S6). The peak at 1737 cm^{-1} in the neat samples arises from the carbonyl stretch (C=O bond), and lithium ion coordination with the methacrylate group should result in red-shifting of this peak.[44,45] The salt blended samples (blue curves in Fig. 4b) for POEM$_9$ and POEM$_5$ show no change whatsoever from the neat samples. The r = 0.05 POEM$_3$ samples does exhibit a small secondary peak near 1710 cm^{-1}, suggesting that some carbonyl oxygens do interact with lithium ions. The size of the low wavenumber peak is much smaller than that of the free C=O peak at 1731 cm^{-1}, however, so the total fraction of lithium-carbonyl complexes in the systems is likely quite low.[46,47] Shifts in several of the characteristic ether side-chain peaks (C-O-C symmetric stretch at 1101 cm^{-1}, CH$_2$ wagging at 1352 cm^{-1}) indicate that Li$^+$ ions instead coordinate with ether oxygens, though the overlap of these peaks with those of the TFSI anion make direct comparison of the neat and r = 0.05 systems difficult.[48] This is consistent with previous reports where it has been shown that in materials with both carbonate and ether functionalities, Li$^+$ ions may be preferentially coordinated with the C=O group if the ether chains contain only one or two oxygens.[49,50] Once there are at least three EO units in a chain however, the polyether chain can form a chelating structure around the Li$^+$ ion, and this solvation is favored over the C=O group association. These FTIR data are entirely consistent with the MD results, and we can confidently conclude that the vast majority of ion solvation sites are comprised of ether oxygens in all linear and graft polymers studied here. These results validate our use of constant r ([Li]/[EO]) for this study, though this strong preference for ether oxygen association may impose limitations on Li$^+$ ion conduction pathways throughout the system.

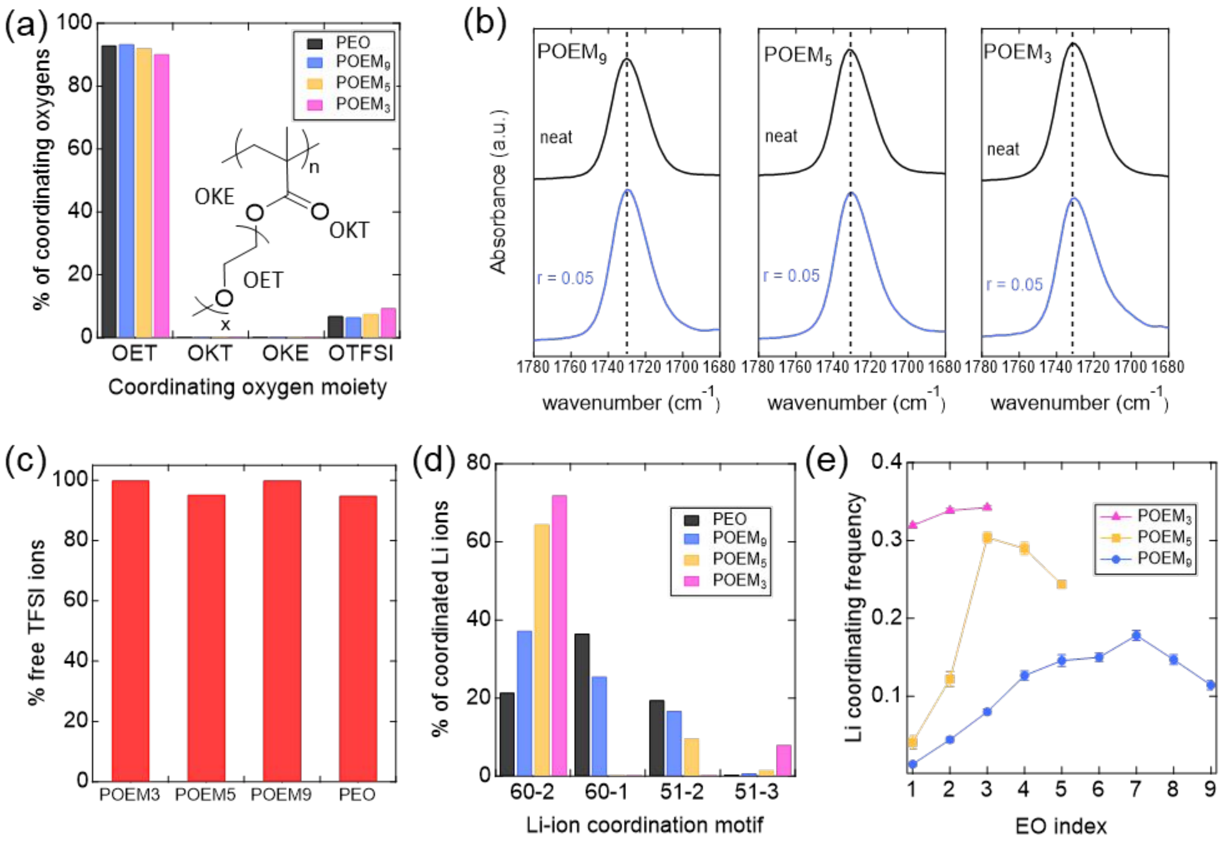

Fig. 4. Ionic association and solvation. (a) Relative percentage of solvating oxygen of each type from MD simulations (ether oxygen – OET, carbonyl oxygen – OKT, ester oxygen – OKE, TFSI^- ion – OTFSI); (b) experimental FTIR spectra of the carbonyl (C=O) stretch for neat and $r = 0.05$; (c) percentage of free ions in $r = 0.05$ electrolyte systems as determined from Raman spectroscopy; (d) percent occurrence of most common solvation motifs (XY-Z refers to solvation by X ether oxygens, Y TFSI^- oxygens, involving Z polymer chains plus TFSI^- anions) from simulation; and (e) percent occurrence of solvation by a given ether oxygen along the POEM side-chain from simulation.

The MD results also suggest that the prevalence of Li-TFSI complexation is low, with fewer than 10% of all solvating oxygen atoms coming from TFSI^- in any given system. To experimentally confirm the absence of a large number of associated species which may reduce ionic conductivity, we use Raman spectroscopy to probe molecular vibrations of the TFSI molecule. Raman spectra for PEO and POEM $r = 0.05$ systems in the range of 720 – 760 cm^{-1} are shown in Fig. S7. The peak in this range can be fit to a free TFSI anion peak at 741 cm^{-1} and an associated anion peak at 744 cm^{-1} to estimate a fraction of free ions in the system.[51,52] The percentage of free ions in the system is taken from the area fraction of the fitted Voigt peaks and plotted in Fig. 4c. For all four polymer systems, the free ion content is nearly 100%, within error of the peak fitting. Although the simulations suggest that there may be a greater fraction of TFSI in the Li^+ solvation shells, the Raman data suggest that these interactions are extremely weak and do not constitute ion pairs or higher order aggregates. We can assume that the ions are fully dissociated, and lithium only briefly interacts with counterions that make up a small fraction of any given solvation site. Differences in the degree of ionic dissociation is therefore not expected to be a significant contributor to the decrease in conductivity observed in short side-chain POEM.

Although the degree of solvation is quantitatively similar for all four materials, the solvation environment may be qualitatively different for each, based on the amount and configuration of ether oxygens in the system. Atomistic MD simulations allow us to further characterize these polymer electrolyte systems by the structure of individual solvation sites at the molecular level. Fig. 4d shows the relative propensity for the four most common solvation motifs in each polymer system. Several of these most common solvation motifs are shown as simulation snapshots in Fig. 1b. Coordination motifs are denoted by “XY-Z”, where X refers to the number of ether oxygens in the first solvation shell, Y refers to the number of TFSI molecules in the first shell, and Z is the number of polymer chains plus TFSI anions present in the solvation shell. For example, the 51-2 motif refers to coordination by five ether oxygens from a single chain and one

TFSI anion. For POEM, each side-chain is considered separately, and in PEO, although it is a single long chain, we consider noncontiguous segments of the backbone to be separate chains for this purpose. We find that the most common motifs all involve either five or six ether oxygens, consistent with previous findings that this represents the most stable configurations for cation coordination.[30,53,54] However, certain motifs are inaccessible to some polymer systems, such as the 60-1 motif (six ether oxygens from a single chain). This configuration is the most likely for PEO and is also readily adopted by $POEM_9$, though it cannot occur in $POEM_5$ or $POEM_3$. Instead, these shorter side-chain systems exhibit a greater prevalence of the 60-2 configuration, creating the six-oxygen solvation shell from three oxygens each from two side-chains. Although Li^+ ions are solvated in a qualitatively similar manner across all four polymer systems studied, the local polymer conformations adopted to create those solvation shells is highly dependent on the chain architecture and conformation.

The strong preference for specific solvation motifs gives rise to heterogeneity along the side-chains of POEM, with some oxygens participating in solvation significantly more frequently than others. Fig. 4e shows the prevalence of ionic association with specific ether oxygens in POEM as a function of distance along the side-chain. EO units are indexed from 1 being the unit closest to the methacrylate group. In $POEM_3$, all oxygens participate at roughly the same frequency, as there are no ways to produce the 60-2 motif (>70% of the solvation structures) without involving all three ether oxygens of a given side-chain. However, both $POEM_5$ and $POEM_9$ exhibit much higher likelihood of coordination by EO units farther from the backbone, with units 3-5 and 4-9, respectively, being significantly overrepresented in solvation. This can be understood by two combined effects. First, there are more permutations of three (or six) contiguous ether oxygens in the middle of the side-chain, and so those EO units are statistically more likely to be involved in solvation. Second, the EO units near the backbone are in very close proximity to the methacrylate group which does not participate in solvation. This limits the ability of those EO units to come close enough to EO units of another chain to form a full solvation shell. This heterogeneity in ether oxygen involvement is a direct result of the graft chain architecture, and the relative contribution of each ether oxygen to ion transport may not be equal.

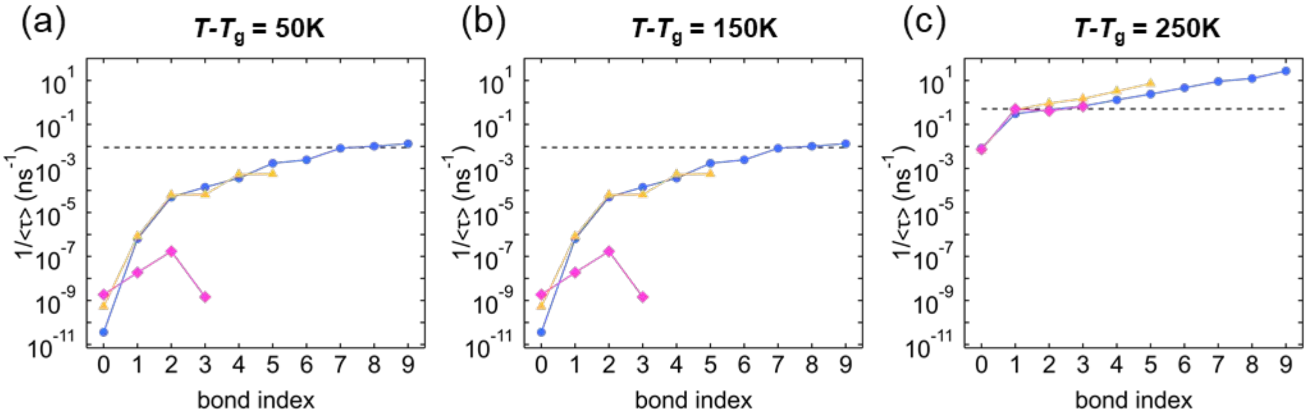

Fig. 5. Inverse mean relaxation time ($1/\langle\tau\rangle$) of different bonds along the polymer chains at (a) T-T_g = 50K, (b) T-T_g = 150K, and (c) T-T_g = 250K derived from the bond vector autocorrelation function. $1/\langle\tau\rangle$ serves here as an indicator of local segmental mobility. Index 0 is the C-C bond along polymer backbone. The other indices refer to the C-O bonds in the ether side chain with index 1 being the closest to the backbone. The solid colored lines are to guide the eye.

Graft chain architecture results in heterogeneous polymer dynamics

The selective solvation by certain EO repeat units in the graft polyethers suggest that only part of the polymer chains meaningfully contribute to the measured ionic conductivity. This may explain why metrics such as T_g and solvation site density, which are system wide average values, do not fully capture the transport behavior. Instead, a more nuanced, local understanding of segmental dynamics and solvation is warranted. Rather than using macroscopic averages of segmental mobility by DSC, we can instead use the MD trajectories to determine the local mobility of individual ether oxygen units. Fig. 5 shows the inverse mean relaxation time, $1/\langle\tau\rangle$, extracted from the C-O bond vector autocorrelation function (BVAF) at different T-T_g as a function of position along the polymer side-chain. Detailed explanation of this calculation are provided in the Supporting Information. Briefly, the BVAF describes how quickly neighboring bonds decorrelate from an initial orientation. The mean relaxation time can be fit to a stretched exponential function, and $1/\langle\tau\rangle$ serves as an indicator of local segmental mobility. This analysis was introduced in our previous work, and the methodology is described in greater detail there.[34]

In the linear PEO system, $1/\langle\tau\rangle$ shows no dependence on ether oxygen position, as 150 kg mol^{-1} molecular weight used in the simulation is well above the chain length where chain ends ought to impact local dynamics or conductivity for most ether units.[55] In all three POEM systems, conversely, the local dynamics are strongly dependent on bond index. Those units closest to the polymer backbone exhibit significantly suppressed dynamics relative to PEO, while EO monomers near the side-chain end decorrelate at an equal or greater rate than PEO. This trend arises from similar competing effects that were attributed to difference in ion complexation by different EO positions. The C-C backbone carbon bond (bond index 0) exhibits between six and eight orders of magnitude slower relaxation rates than PEO, and the POEM ether units near this low mobility backbone have similarly suppressed dynamics. The POEM ether units farthest from the backbone, however, have greater free volume to sample, and exhibit faster dynamics as a result. Importantly, all of the $1/\langle\tau\rangle$ in Fig. 5 are determined at fixed temperature above the respective T_g of each polymer. Any differences in the average mobility of ether oxygens between the different systems, therefore, are not captured by T_g, and these differences may explain the observed ionic conductivity behavior.

In addition to the clear importance of ether oxygen placement along the side-chain, the relaxation time of a given POEM EO unit relative to that of PEO is strongly dependent of temperature. In Fig. 5a, at T-T_g = 50 K, the mobility of the backbone and EO units near it are several orders of magnitude slower than PEO at the same relative temperature, and only EO units 7-9 in POEM$_9$ have 1/<τ> equal to or greater than PEO. At 250 K above T_g, on the other hand, the backbone only has two orders of magnitude longer relaxation time than PEO, and essentially all ether units in the POEM systems relax as fast or faster than the linear PEO. This temperature dependence is likely due to rapidly increasing dynamics of the POEM backbone with temperature. As a reference point, the T_g of poly(methyl methacrylate), which is chemically equivalent to the POEM without the polyether side-chain, is around 100 °C compared to -50 °C for PEO. The dynamics of polymers tends to increase most rapidly at temperatures at and just above the glass transition, with relatively more modest increases in mobility with temperature at large values of T-T_g.[56] This same effect is evident in these graft polymer systems where the lower mobility backbone sees much greater increase in local segmental dynamics than the already high mobility side-chains with the same increase in temperature.

This local heterogeneity in segmental mobility may reconcile the discrepancy between κ/κ_{PEO} and σ_{nr} discussed earlier (Fig. 3). At intermediate T-T_g the average mobility of the EO units in POEM is quite similar to that of PEO, and differences in T_g accurately capture the important dynamics in the system. As a result, after normalization by T-T_g, solvation site connectivity accurately captures the differences in conductivity as a function of POEM side-chain length. At high temperatures, many of the ether oxygens most often involved in ion complexation are more mobile than the linear PEO, and the T_g of the graft system does not adequately describe the important segmental dynamics. σ_{nr} therefore overpredicts the solvation site connectivity because normalization by T_g fails to account for the fast ether oxygens at the side-chain ends. This effect is more pronounced in the longer side chain materials, as there are more of these fast ether units present. In POEM$_3$ even the furthest EO unit from the backbone is still affected by the main-chain dynamics and is only marginally more mobile than PEO. In POEM$_9$, on the other hand, six of the nine side-chain oxygens exhibit faster local segmental mobility than PEO. Conversely, the dynamics of many of the most commonly solvating ether units in POEM are considerably slower than PEO at low temperatures. Here the ionic conductivity is limited by the slow dynamics of the methacrylate backbone. In this case σ_{nr} falls short of the solvation site connectivity prediction because the important dynamics in the system are slower than what is captured by the overall material conductivity. Again, the POEM$_3$ is the system most negatively impacted by the low mobility of the methacrylate backbone, whereas the highest index EO units of POEM$_9$ reach or exceed the relaxation rate of PEO. These results suggest that local segmental dynamics of the polymer side-chain are at least as important as T_g, ionic dissociation, and solvation site connectivity in determining ionic conductivity in graft polyethers. Both backbone flexibility and side-chain length are critical parameters in designing materials with rapid ionic transport.

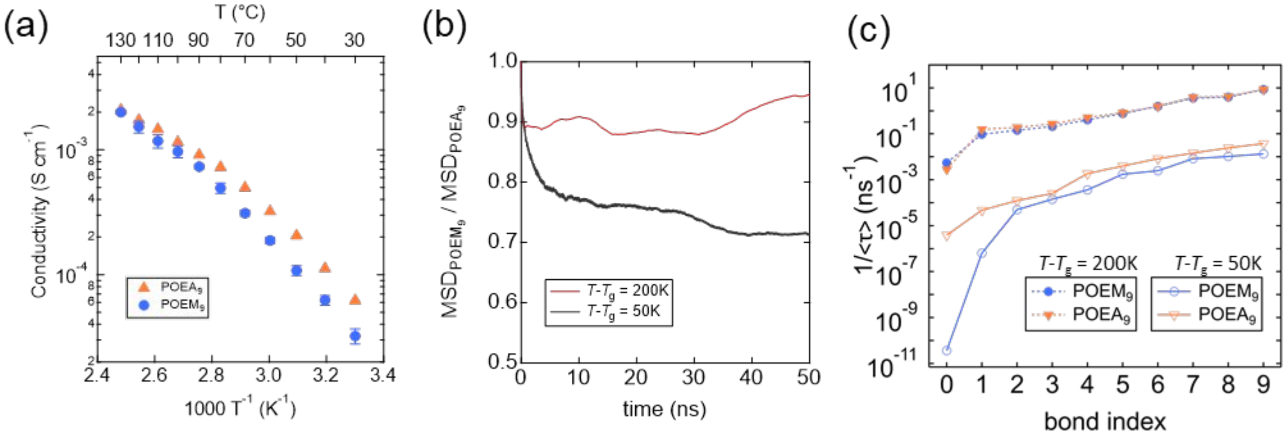

Fig. 6. (a) Temperature dependent conductivity (experiment), (b) Ratio of Li^+ ion MSD, and (c) inverse mean relaxation time in $POEA_9$ compared to $POEM_9$ (simulation).

To validate this model for ion transport in graft polyethers, two more materials were synthesized and characterized. $POEA_9$, the polyacrylate analogue to $POEM_9$, and a random copolymer, $POEM_9$-*r*-PMMA, with the same x_{EO} as $POEM_3$ were synthesized by the same RAFT polymerization as described previously. The experimental conductivity, Li^+ ion MSD *vs* time, and local BVAF decorrelation times for $POEA_9$ and $POEM_9$-*r*-PMMA at $r = 0.05$ are shown in Fig. 6. From Fig. 6a, we can see that the $POEA_9$ conductivity exceeds that of $POEM_9$ at low temperatures by a factor of more than three, but the conductivity of the two systems converge above *ca*. 100 °C. Although we measure the T_g of the two systems to be relatively similar (see Table 1), the polyacrylate backbone should be more flexible than the polymethacrylate one, as T_g of poly(methyl acrylate) is *ca.* 5 °C, well below that of polymethyl methacrylate. Previous bottle-brush copolymer systems based on POEA have been shown to exhibit higher ionic conductivity than similar systems incorporating POEM.[57] That the conductivity of these two systems converges at high temperature, however, is consistent with the hypothesis that backbone dynamics become less significant to ion transport at higher temperatures. At these elevated temperatures the difference between the relaxation times in the polyacrylate and polymethacrylate backbones is small, and the identical nature of the two side chains results in similar ionic conductivity values. These experimental observations are confirmed by MD simulations, where we find a similar temperature dependence in the ratio of Li^+ ion MSD in $POEA_9$ to that in $POEM_9$ (Fig. 6b). At T-T_g = 200 K, the ratio of Li^+ ion MSD in $POEM_9$ to that of $POEA_9$ is 0.9 or greater, while at T-T_g = 50 K the ratio is ca. 0.7. Additionally, as seen in Fig. 6c, the $POEM_9$ backbone relaxes significantly more slowly than the

POEA$_9$ backbone at low temperatures, with $1/\langle\tau\rangle$ several orders of magnitude higher in the methacrylate polymer. This difference in backbone relaxation rate results in a persistently faster local relaxation rate in POEM compared to POEA at T-T_g = 50 K for all ether oxygens. At T-T_g = 200 K, conversely, the backbone relaxation rates are identical in both systems, as are the dynamics of all ether oxygens in the two materials. Clearly, at these elevated temperatures the acrylate and methacrylate backbones both relax relatively quickly compared to the ether side-chain, and the effect of the backbone is minor in determining the material conductivity.

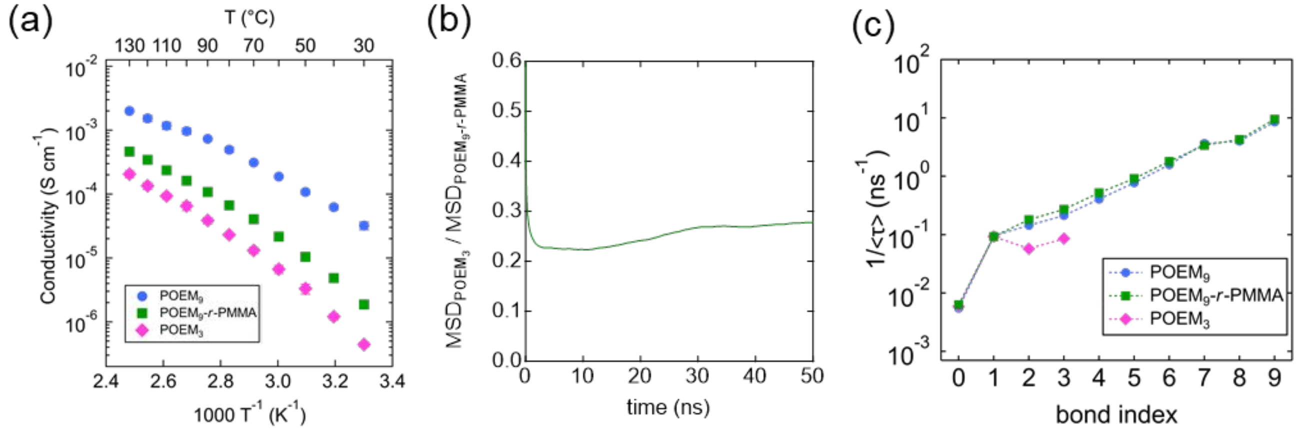

Fig. 7. (a) Temperature dependent conductivity (experiment), (b) Ratio of Li^+ ion MSD, and (c) inverse mean relaxation time in POEM$_9$-*r*-PMMA compared to POEM$_3$ and POEM$_9$ (simulation).

A POEM$_9$-*r*-PMMA copolymer was synthesized with an ether oxygen fraction similar to that of POEM$_3$ to validate the importance of side-chain length—and not just x_{EO}—in determining conductivity. Fig. 7a shows the experimental conductivity for these two systems. The random copolymer exhibits consistently higher ionic conductivity, by approximately three-fold, irrespective of temperature. This behavior is not explained by the modest differences in measured T_g of the two systems, nor is it captured by differences in solvation site density and connectivity, which depends primarily on x_{EO}. Instead, this behavior can be explained only by the outsized importance of EO units far from the backbone can have on ion transport within graft polymers. Whereas the POEM$_3$ consists of densely packed but extremely short side-chains, the POEM$_9$-*r*-PMMA system contains a lower density of side-chains with mobile ether oxygens far from the backbone. Although the presence of randomly distributed, nonconducting PMMA units clearly disrupts the solvation network and negatively effects the material conductivity, this dilution effect is significantly less severe than the absence of any long side-chains capable of rapid segmental mobility. These findings are again confirmed by MD simulations. The ratio of Li^+ ion MSD of POEM$_9$-*r*-PMMA to POEM$_3$ (Fig. 7b) closely matches the ratio of experimentally determined conductivity (*ca.* 2.6-3.2 from experiment, and 2.8 at 50 ns from simulation). The local segmental mobility analysis (Fig. 7c) similar validates this understanding of the differences between these two materials. Although the connectivity between the solvation sites should be similar between the two systems based on their similar ether oxygen content, the mobility of the POEM$_9$ is unperturbed by the presence of PMMA. The local mobility of the EO units furthest from the backbone remain much more flexible than those in POEM$_3$, and as a result are capable of facilitating more rapid ionic transport.

Implications for the design of polyether-based polymer electrolytes

These results underscore the critical relationship between polymer dynamics and ion transport that must be understood when measuring and analyzing new ion conducting materials, particularly those based on short side-chain ether units. We have clearly demonstrated that a single value for T_g does not account for the local heterogeneity in oxygen mobility in these side-chain systems, and it does not fully capture the relevant dynamics for producing fast ionic transport. While there are differences in the T_g of the graft polyethers examined in this study, these differences were negligible relative to the orders of magnitude different measured ionic conductivities. The observed difference in ionic conductivity was largely related to segmental dynamics, but DSC measurements failed to capture the local nature of these dynamics. The discrepancy between segmental dynamics measured by DSC and simulations highlight the importance of other experimental techniques, such as quasi-elastic neutron scattering, to probe the relevant local dynamics of these systems.[58–60] Moreover, the oxygens most likely to be involved in solvation (*i.e.* those towards the side-chain ends) were more mobile than the polymer average, giving rise to fast conduction without exhibiting a low T_g. On the other hand, materials that lack those mobile oxygens due to having only short ether side-chains were limited by the relatively low mobility backbone. Though all materials studied here exhibit a glass transition well below room temperature, it is not until around 150 K above T_g that the backbone begins to relax at a rate comparable to the ether side-chains. As a result, many of the EO units close to the backbone are prevented from effectively participating in the conduction mechanism. While side-chain mobility directly controls the conductivity, the side-chain mobility itself is largely dependent on the backbone mobility. Tailoring the connection between the side-chain and backbone to maximize flexibility offers a potential materials design opportunity to optimize the conductivity of these systems.

More generally, although low T_g is conventionally used as a hallmark of a potential candidate for high ionic conductivity, this may not always be a good proxy, and more detailed descriptions of segmental dynamics are necessary. As demonstrated here, such descriptions can be best captured by a combined experimental and computational approach. Local relaxation times, in addition to conventional metrics, such as ether oxygen content, T_g, and ionic dissociation, as well more recently introduced quantifiers, such as solvation site connectivity, must be accurately modeled in order to fully capture the ionic transport behavior of graft polyether electrolytes. Most importantly, it is the local mobility of the segments actively participating in the formation sites, not the overall dynamics of the system, that appears to be critical in limiting the ion conductivity of these materials.

Side-chain length has also been shown to be an important materials design criterion that may apply to a broad range of polyether electrolytes. In linear polyether ion conducting polymers, ether oxygen content and T_g may be used to accurately predict the conductivity of a newly prepared material. In systems where short PEO chains are connected to a polymer backbone, however, we have demonstrated that the flexibility of the main chain and its effect on the mobility of side chain ether units, as well as the length of the PEO chains have an outsized effect on the overall ionic conductivity. The role of backbone flexibility has significant implications for the development of graft copolymers based on POEM or POEA repeat units that represent an important class of potential lithium battery electrolyte membranes with a wide potential design window.[16] Even broader polymer chemistry is available in the development of bottlebrush polymer electrolytes, where the ion conducive side-chains can be incorporated by a graft-to or graft-through synthetic approach.[12,61,62] With this synthetic flexibility, the choice of backbone of chemistry and side-chain linkages may be tailored to maximize ether side-chain dynamics, such as polysiloxane or polyphosphazene main chains.[63,64] Another technologically relevant system that makes use of short, periodically spaced PEO chains connected to less flexible moieties is crosslinked polyether binder materials.[65] Further investigation is warranted to explore how these ideas of local ether oxygen mobility affect conductivity in systems where ether chains are tethered at both ends, or in the case of dynamic crosslinked networks, one or both chain ends is covalently linked to a crosslinking site.[21] Finally, dual ion-electron conducting polymers of interest for lithium ion battery applications often make use of ether side-chains covalently bonded to an electronically conductive conjugated backbone.[66] In these systems, the ion conductivity will likely be significantly affected by the length of ether side chain and type of covalent linkage to the rigid thiophene backbone.[23] In these systems, and in all ion conducting polymers based on nonlinear polyethers, the interplay between polymer composition and architecture, backbone rigidity, and side-chain relaxation rates will play a critical role in determining the temperature dependent conductivity behavior.

Conclusions

In this study we have clarified the relationship between side-chain length, ion solvation, segmental dynamics, and ionic conductivity in graft polyether electrolytes. Ionic conductivity of $POEM_9$ was found to be more than an order of magnitude higher than in $POEM_3$ even after correcting for differences in T_g. This behavior was partially explained by solvation site connectivity, but a temperature dependence in the normalized conductivity could not be reconciled by this approach. MD simulations and vibrational spectroscopy found that ions were fully dissociated in all systems, but dissolved Li^+ ions were found to preferentially reside in the ether side chains, rather than associating with the carbonyl groups in the methacrylate backbone. Moreover, ether units furthest from the backbone were most likely to coordinate with Li, suggesting that these units have an outsized effect on the formation of solvation sites and in facilitating ionic motion. Most importantly, these same ether oxygen atoms at side-chain ends exhibited much faster dynamics than those near the methacrylate backbone, and this effect explained both the trend in conductivity as a function of side-chain length as well as the temperature-dependent normalized conductivity behavior. These differences in C-O bond relaxation rates were not captured by differences in T_g, and therefore T_g alone may not be a good proxy for the relevant polymer dynamics resulting in high ionic conductivity in graft polymer electrolytes. Instead, the mobility of the EO segments that participate in solvation site formation is the most critical factor, and the dynamics of non-participating segments is secondary.

From the results presented here, several important design criteria can be proposed. First, more mobile backbone moieties can be introduced to improve the low temperature conductivity of graft polymer electrolytes. This was exemplified by comparing otherwise equivalent acrylate and methacrylate graft polyethers, where the acrylate exhibited three-fold higher conductivity at room temperature. This effect was minimal at higher temperatures, however, once the backbone dynamics approached those of the ether side-chains. Improvement to the conductivity at all temperatures was shown in a random copolymer based on long side-chains compared to that of a compositionally identical polymer with shorter side-chains. The important material parameter here was shown to be the presence of mobile oxygens at the side-chain ends, not the overall ether oxygen content. Finally, the solvation properties and segmental dynamics should be considered at a local, rather than global scale, when designing new ion conducting polymers based on short EO chains. Here, atomistic MD simulations, coupled with experimental characterizations, provided deeper insight into the important mechanisms of ion transport in these systems, and future materials design may be accelerated by taking this combined approach.

Experimental Methods

Materials

PEO was purchased from Polymer Source, Inc. and dried in an argon glovebox antechamber at 50 °C overnight before use. All other chemicals—acetonitrile (99.8%, anhydrous), toluene, dimethylformamide (DMF), tetrahydrofuran (THF), hexanes, diethyl ether, LiTFSI (battery grade, >99.95% trace metal basis), 2-cyano-2-propyl dodecyl trithiocarbonate (CPDTC), azobisisobutyronitrile (AIBN), and all monomers—were purchased from Sigma Aldrich. Oligo(ethylene oxide) methyl ether methacrylate (OEM$_x$, where $x = 3$, 5, or 9; $M_\mathrm{n} = 232$, 300, or 500 g mol^{-1}), methyl methacrylate (MMA), and oligo(ethylene oxide) methyl ether acrylate (OEA$_9$, $M_\mathrm{n} = 475$ g mol^{-1}) were purified of inhibitor before use by passing through a column of basic alumina. LiTFSI was further under vacuum at 100 °C for 48 h. Polymers and LiTFSI were stored in an argon glovebox after the drying processes. AIBN was recrystallized in ethanol before use.

***Synthesis of POEM$_x$ and POEA$_9$ homopolymers*-** POEM$_x$ and POEA$_9$ homopolymers were prepared by RAFT polymerization according to Scheme S1. For the synthesis of POEM$_9$, 5 g (10 mmol) of OEM$_9$ monomer was placed in a round bottom flask along with 0.17 g (0.5 mmol) CPDTC, 8.2 mg (0.05 mmol) of AIBN, and 9.8 mL of DMF. The flask was sealed with a rubber septum and the solution sparged with dry N_2 for 30 minutes. The flask was then placed in an oil bath at 70 °C for 20 hours, after which it was quenched in an ice water bath. The crude reaction mixture was concentrated under vacuum and then diluted with THF. This polymer was then precipitated from cold diethyl ether or a mixture of diethyl ether and hexanes. This purification process was repeated three times, or until ^{1}H-NMR spectra showed no residual monomer in the material. Purified polymer was then dried in a vacuum oven to a constant mass and then further dried under high vacuum for 24 hours before storing in an argon glovebox. The other homopolymers were prepared in a similar manner.

Synthesis of POEM-r-PMMA random copolymer- POEM$_9$-*r*-PMMA was synthesized according to Scheme S2 following the same general procedure as the homopolymer materials. 3.5 g (7 mmol) of OEM$_9$, 1.5 g (15 mmol) of MMA, 0.17 g (0.5 mmol) CPDTC, 8.2 mg (0.05 mmol) of AIBN, and 9.8 mL of DMF were combined in a round bottom flask, sealed with a rubber septum, sparged with dry N_2, and placed in a 70 °C oil bath for 20 hours. The crude solution was purified by the same process as the homopolymers. The ratio of OEM$_9$:MMA in the resulting polymer was determined by ^{1}H-NMR. The NMR spectrum and peak comparison is Fig. S8.

Polymer electrolyte solution preparation- Polymer solutions were prepared inside of an argon glovebox by dissolving polymer in either pure acetonitrile or a mixture of acetonitrile and toluene (50/50 v/v). Solutions were heated to 50 °C to help facilitate dissolution of the polymer and then were left stirring overnight. LiTFSI in acetonitrile solutions were prepared in the same manner. Polymer electrolyte solutions were prepared by blending polymer and salt solutions at an appropriate volumetric ratio to obtain a ratio of $r = 0.05 = [\text{LiTFSI}]/[\text{EO}]$.

Materials Characterization

Size exclusion chromatography (SEC)- Size exclusion chromatography (SEC) measurements were conducted on a Shimadzu Prominence High Performance Liquid Chromatograph system with THF as eluent at a flow rate of 1 mL/min. Separation was achieved using two PLgel mixed-D columns (Agilent) maintained at ambient temperature. The differential refractive index signal was collected using a Wyatt Optilab T-rEX differential refractometer (λ = 658 nm). On-line multi-angle light scattering (MALS) measurement was performed using a Wyatt Dawn Heleos II light scattering detector. Weight-averaged molecular weight and dispersity were determined by MALS using the previously reported refractive index increment for POEM9 in THF (*dn*/*dc* = 0.073 mL/g).[67]

Determination of copolymer composition by ^{1}H-NMR- POEM$_9$-*r*-PMMA copolymer composition was determined by ^{1}H-NMR in $CDCL_3$. Data were acquired on a 500 MHz Bruker Avance-II+ spectrometer equipped with a ^{1}H QNP probe, using Topspin 2.1. Copolymer composition was determined by comparing the methacrylate backbone methyl group peaks (δ = 0.7 – 1.5 ppm) to the methyl ether peaks at the end of the POEM$_9$ side-chain (δ = 3.38 ppm).[68] The copolymer was determined to have a POEM$_9$ mole fraction of 0.273.

Differential Scanning Calorimetry- Calorimetric glass transition temperatures (T_g) of neat polymers and polymer electrolytes were determined by DSC using a TA Instruments Discovery 2500 DSC. Sample pans were prepared in the glovebox by drop casting solutions, heating at 65 °C until dry, and then repeating until 5 – 10 mg of material was in the pan. The pans were then hermetically sealed before removing from the glovebox to avoid any water adsorption before DSC measurement. Samples were conditioned at 135 °C followed by three cycles of cooling to -85 °C and heating to 135 °C at a scan rate of 10 °C/min. T_g is reported as the inflection point of the heat flow thermograms taken from the third heating curve (shown in Fig. S3).

Vibrational Spectroscopy- Samples for Fourier Transform Infrared (FTIR) measurements were prepared on Au-coated Si substrates by spin coating. Samples were prepared inside of a glovebox, annealed at 135 °C for 15 minutes, and sealed then until immediately before measurement to minimize water absorption. Measurements were performed using a Shimadzu IRTracer-100 spectrometer using a diamond prism for attenuated total reflection (ATR) at ambient temperature from 400 – 4000 cm^{-1} at a resolution of 4 cm^{-1}. Raman samples were prepared by drop casting films on Au-coated Si substrates inside of a glovebox. Films were dried and then annealed at 135 °C for 15 minutes inside of the glovebox and then sealed until measurement. Raman experiments were performed using a Horiba LabRAM HR Evolution NIR confocal Raman microscope. Raman spectra were collected with a 100x objective and a 633 nm wavelength laser.

Thin film conductivity measurements- Polymer electrolyte conductivity was determined by electrochemical impedance spectroscopy (EIS) of thin films on interdigitated electrodes (IDEs) as described previously.[69] Briefly, IDEs are microfabricated by photolithography on top of thermal oxide Si wafers. 5 nm of Ti followed by 45 nm of Au are deposited in the lithographically defined electrode area, and excess metal is removed by liftoff in warm *n*-methyl pyrrolidone. IDEs are designed with $N = 160$ electrodes, $l = 1$ mm of electrode overlap, $w = 2$ µm electrode width, and $d = 8$ µm interelectrode distance. IDEs were then coated with 0.8 nm of SiO_2 by plasma-assisted atomic layer deposition to inhibit dewetting of the polymer films. Polymer electrolyte thin films were cast onto the IDEs by spin coating at 4000 rpm inside of the glovebox, followed by drying on a hot plate at 70 °C before EIS measurements. Polymer film height (h) was determined by casting an identical film on a Si wafer and performing ellipsometry (J.A. Woollam alpha-SE ellipsometer). IDEs were placed on a custom heating stage in the glovebox and connected to a Gamry 600+ potentiostat by tungsten probe tips. Potentiostatic EIS was performed with an applied amplitude of 100 mV over a frequency range of 1 MHz to 1 Hz. EIS data is fit to an appropriate equivalent circuit that models the physical process of thin film-IDE systems using the Gamry E-chem Analyst software, and the resulting film resistance (R_f) is used to find the conductivity (σ) by *eq.* 3.[70] All conductivity data is reported as the average of three samples, with error bars representing the standard deviation.

$$\sigma = \frac{d}{R_f(N-1)lh} \qquad (2)$$

Molecular Dynamics Simulations

The polymers are represented by united atoms, using an adapted Trappe-UA force-field[71–73] that has been previously validated to match the density of PEO[74]. Li^+ and $TFSI^-$ ions are represented by a compatible all-atom model[75]. A cutoff radius of 12 Å is used for short range non-bonded interactions. Long range non-bonded interactions use a cutoff radius of 12 Å and are handled using the Particle-particle particle-mesh solver[76] with 10^{-4} accuracy. The simulation is conducted using the LAMMPS package[77]. The velocity-Verlet integrator with a 1 fs timestep is used. For NVT simulations, the Nose-Hoover thermostat with a damping parameter of 100 fs is used. For NPT simulations, the Nose-Hoover barostat with a damping parameter of 1000 fs is used. Additional details of the simulation procedures and force field parameters are included in the Supporting Information.

Conflicts of Interest

There are no conflicts to declare.

Acknowledgments

We gratefully acknowledge support by the U.S. Department of Energy (DOE), Basic Energy Sciences, Materials Sciences and Engineering Division. This work made use of the Pritzker Nanofabrication Facility of the Institute for Molecular Engineering at the University of Chicago, which receives support from Soft and Hybrid Nanotechnology Experimental (SHyNE) Resource (NSF ECCS-1542205), a node of the National Science Foundation's National Nanotechnology Coordinated Infrastructure. We acknowledge the MRSEC Shared User Facilities at the University of Chicago (NSF DMR-1420709). Parts of this work were carried out at the Soft Matter Characterization Facility of the University of Chicago. The simulations were completed on computational resources provided by the University of Chicago Research Computing Center. MAW acknowledges support from Princeton University.

References

1 Z. Xue, D. He and X. Xie, *J. Mater. Chem. A*, 2015, **3**, 19218–19253.

2 Y. Tominaga, *Polym. J.*, 2017, **49**, 291–299.

3 T. Morioka, K. Nakano and Y. Tominaga, *Macromol. Rapid Commun.*, 2017, **38**, 1600652.

4 S. D. Tillmann, P. Isken and A. Lex-Balducci, *J. Power Sources*, 2014, **271**, 239–244.

5 D. M. Pesko, Y. Jung, A. L. Hasan, M. A. Webb, G. W. Coates, T. F. Miller and N. P. Balsara, *Solid State Ionics*, 2016, **289**, 118–124.

6 J. Mindemark, B. Sun, E. Törmä and D. Brandell, *J. Power Sources*, 2015, **298**, 166–170.

7 T. Uno, S. Kawaguchi, M. Kubo and T. Itoh, *J. Power Sources*, 2008, **178**, 716–722.

8 M. D. Galluzzo, W. S. Loo, A. A. Wang, A. Walton, J. A. Maslyn and N. P. Balsara, *J. Phys. Chem. B*, 2020, **124**, 921–935.

9 M. A. Morris, S. H. Sung, P. M. Ketkar, J. A. Dura, R. C. Nieuwendaal and T. H. Epps, *Macromolecules*, 2019, **52**, 9682–9692.

10 G. Jo, H. Jeon and M. J. Park, *ACS Macro Lett.*, 2015, **4**, 225–230.

11 R. Bouchet, S. Maria, R. Meziane, A. Aboulaich, L. Lienafa, J. P. Bonnet, T. N. T. Phan, D. Bertin, D. Gigmes, D. Devaux, R. Denoyel and M. Armand, *Nat. Mater.*, 2013, **12**, 452–457.

12 C. M. Bates, A. B. Chang, N. Momčilović, S. C. Jones and R. H. Grubbs, *Macromolecules*, 2015, **48**, 4967–4973.

13 S. Li, K. Jiang, J. Wang, C. Zuo, Y. H. Jo, D. He, X. Xie and Z. Xue, *Macromolecules*, 2019, **52**, 7234–7243.

14 Z. Geng, N. S. Schauser, J. Lee, R. P. Schmeller, S. M. Barbon, R. A. Segalman, N. A. Lynd and C. J. Hawker, *Macromolecules*, , DOI:10.1021/acs.macromol.0c01116.

15 P. P. Soo, B. Huang, Y. I. I. Jang, Y. M. Chiang, D. R. Sadoway and A. M. Mayes, *J. Electrochem. Soc.*, 1999, **146**, 32–37.

16 W. F. Kuan, R. Remy, M. E. Mackay and T. H. Epps, *RSC Adv.*, 2015, **5**, 12597–12604.

17 J. Shim, F. S. Bates and T. P. Lodge, *Nat. Commun.*, 2019, **10**, 2108.

18 S. W. Ryu, P. E. Trapa, S. C. Olugebefola, J. A. Gonzalez-Leon, D. R. Sadoway and A. M. Mayes, *J. Electrochem. Soc.*, 2005, **152**, A158.

19 C. T. Elmore, M. E. Seidler, H. O. Ford, L. C. Merrill, S. P. Upadhyay, W. F. Schneider and J. L. Schaefer, *Batteries*, 2018, **4**, 28.

20 L. Porcarelli, A. S. Shaplov, M. Salsamendi, J. R. Nair, Y. S. Vygodskii, D. Mecerreyes and C. Gerbaldi, *ACS Appl. Mater. Interfaces*, 2016, **8**, 10350–10359.

21 R. Kato, P. Mirmira, A. Sookezian, G. L. Grocke, S. N. Patel and S. J. Rowan, *ACS Macro Lett.*, 2020, **9**, 500–506.

22 B. B. Jing and C. M. Evans, *J. Am. Chem. Soc.*, 2019, **141**, 18932–18937.

23 B. X. Dong, C. Nowak, J. W. Onorato, J. Strzalka, F. A. Escobedo, C. K. Luscombe, P. F. Nealey and S. N. Patel, *Chem. Mater.*, 2019, **31**, 1418–1429.

24 C. B. Nielsen, A. Giovannitti, D. T. Sbircea, E. Bandiello, M. R. Niazi, D. A. Hanifi, M. Sessolo, A. Amassian, G. G. Malliaras, J. Rivnay and I. McCulloch, *J. Am. Chem. Soc.*,

2016, **138**, 10252–10259.

25 S. Lascaud, M. Perrier, A. Vallée, S. Besner, J. Prud'homme and M. Armand, *Macromolecules*, 1994, **27**, 7469–7477.

26 O. Borodin and G. D. Smith, *Macromolecules*, 2006, **39**, 1620–1629.

27 M. Ebadi, T. Eriksson, P. Mandal, L. T. Costa, C. M. Araujo, J. Mindemark and D. Brandell, *Macromolecules*, 2020, **53**, 764–774.

28 D. M. Pesko, M. A. Webb, Y. Jung, Q. Zheng, T. F. Miller, G. W. Coates and N. P. Balsara, *Macromolecules*, 2016, **49**, 5244–5255.

29 M. A. Webb, B. M. Savoie, Z. G. Wang and T. F. Miller, *Macromolecules*, 2015, **48**, 7346–7358.

30 M. A. Webb, Y. Jung, D. M. Pesko, B. M. Savoie, U. Yamamoto, G. W. Coates, N. P. Balsara, Z. G. Wang and T. F. Miller, *ACS Cent. Sci.*, 2015, **1**, 198–205.

31 J. Rolland, J. Brassinne, J. P. Bourgeois, E. Poggi, A. Vlad and J. F. Gohy, *J. Mater. Chem. A*, 2014, **2**, 11839–11846.

32 K. P. Barteau, M. Wolffs, N. A. Lynd, G. H. Fredrickson, E. J. Kramer and C. J. Hawker, *Macromolecules*, 2013, **46**, 8988–8994.

33 J. Karo and D. Brandell, *Solid State Ionics*, 2009, **180**, 1272–1284.

34 C. Deng, M. A. Webb, P. Bennington, D. Sharon, P. F. Nealey, S. N. Patel and J. J. de Pablo, *Macromolecules*, 2021, acs.macromol.0c02424.

35 D. Sharon, P. Bennington, C. Liu, Y. Kambe, B. X. Dong, V. F. Burnett, M. Dolejsi, G. Grocke, S. N. Patel and P. F. Nealey, *J. Electrochem. Soc.*, 2018, **165**, H1028–H1039.

36 J. B. Goodenough and Y. Kim, *Chem. Mater.*, 2010, **22**, 587–603.

37 D. Bresser, S. Lyonnard, C. Iojoiu, L. Picard and S. Passerini, *Mol. Syst. Des. Eng.*, 2019,

4, 779–792.

38 K. M. Diederichsen, H. G. Buss and B. D. McCloskey, *Macromolecules*, 2017, **50**, 3831–3840.

39 K. M. Diederichsen, H. G. Buss and B. D. McCloskey, *Macromolecules*, 2017, **50**, 3831–3840.

40 H. K. Reimschuessel, *J Polym Sci Polym Chem Ed*, 1979, **17**, 2447–2457.

41 M. Chintapalli, T. N. P. Le, N. R. Venkatesan, N. G. Mackay, A. A. Rojas, J. L. Thelen, X. C. Chen, D. Devaux and N. P. Balsara, *Macromolecules*, 2016, **49**, 1770–1780.

42 D. M. Pesko, M. A. Webb, Y. Jung, Q. Zheng, T. F. Miller, G. W. Coates and N. P. Balsara, *Macromolecules*, 2016, **49**, 5244–5255.

43 S. D. Tillmann, P. Isken and A. Lex-Balducci, *J. Phys. Chem. C*, 2015, **119**, 14873–14878.

44 M. Zaheer, H. Xu, B. Wang, L. Li and Y. Deng, *J. Electrochem. Soc.*, 2020, **167**, 070504.

45 S. Selvasekarapandian, R. Baskaran, O. Kamishima, J. Kawamura and T. Hattori, *Spectrochim. Acta Part A Mol. Biomol. Spectrosc.*, 2006, **65**, 1234–1240.

46 K. Kimura, J. Motomatsu and Y. Tominaga, *J. Phys. Chem. C*, 2016, **120**, 12385–12391.

47 B. Sun, J. Mindemark, E. V. Morozov, L. T. Costa, M. Bergman, P. Johansson, Y. Fang, I. Furó and D. Brandell, *Phys. Chem. Chem. Phys.*, 2016, **18**, 9504–9513.

48 L. H. Sim, S. N. Gan, C. H. Chan and R. Yahya, *Spectrochim. Acta - Part A Mol. Biomol. Spectrosc.*, 2010, **76**, 287–292.

49 J. Mindemark, L. Imholt, J. Montero and D. Brandell, *J. Polym. Sci. Part A Polym. Chem.*, 2016, **54**, 2128–2135.

50 T. Morioka, K. Ota and Y. Tominaga, *Polymer (Guildf).*, 2016, **84**, 21–26.

51 J. Grondin, L. Servant, I. Rey and J. C. Lassegues, *Electrochim. Acta*, 1998, **43**, 1505–1510.

52 D. Brouillette, D. E. Irish, N. J. Taylor, G. Perron, M. Odziemkowski and J. E. Desnoyers, *Phys. Chem. Chem. Phys.*, 2002, **4**, 6063–6071.

53 N. Molinari, J. P. Mailoa and B. Kozinsky, *Chem. Mater.*, 2018, **30**, 6298–6306.

54 G. Mao, M. L. Saboungi, D. L. Price, M. B. Armand and W. S. Howells, *Structure of liquid PEO-LiTFSI electrolyte*, 2000, vol. 84.

55 D. Devaux, R. Bouchet, D. Glé and R. Denoyel, *Solid State Ionics*, 2012, **227**, 119–127.

56 D. J. Plazek and V. M. O'Rourke, *J. Polym. Sci. Part A-2 Polym. Phys.*, 1971, **9**, 209–243.

57 Q. Hu, A. Caputo and D. R. Sadoway, *J. Vis. Exp.*, 2013, 4–6.

58 K. I. S. Mongcopa, D. A. Gribble, W. S. Loo, M. Tyagi, S. A. Mullin and N. P. Balsara, *Macromolecules*, 2020, **53**, 2406–2411.

59 K. I. S. Mongcopa, M. Tyagi, J. P. Mailoa, G. Samsonidze, B. Kozinsky, S. A. Mullin, D. A. Gribble, H. Watanabe and N. P. Balsara, *ACS Macro Lett.*, 2018, **7**, 504–508.

60 W. S. Loo, A. Faraone, L. S. Grundy, K. W. Gao and N. P. Balsara, *ACS Macro Lett.*, 2020, **9**, 639–645.

61 Y. Shibuya, R. Tatara, Y. Jiang, Y. Shao-Horn and J. A. Johnson, *J. Polym. Sci. Part A Polym. Chem.*, 2019, **57**, 448–455.

62 M. Guo, M. Zhang, D. He, J. Hu, X. Wang, C. Gong, X. Xie and Z. Xue, *Electrochim. Acta*, 2017, **255**, 396–404.

63 H. R. Allcock, P. E. Austin, T. X. Neenan, J. T. Sisko, P. M. Blonsky and D. F. Shriver, *Macromolecules*, 1986, **19**, 1508–1512.

64 X. Zhang, J.-C. Daigle and K. Zaghib, *Materials (Basel).*, 2020, **13**, 2488.

65 P. Sutton, M. Airoldi, L. Porcarelli, J. L. Olmedo-Martínez, C. Mugemana, N. Bruns, D. Mecerreyes, U. Steiner and I. Gunkel, *Polymers (Basel).*, , DOI:10.3390/polym12030595.

66 J. W. Onorato and C. K. Luscombe, *Mol. Syst. Des. Eng.*, 2019, **4**, 310–324.

67 H. Hussain, K. Y. Mya and C. He, *Langmuir*, 2008, **24**, 13279–13286.

68 D.-G. Kim, H. Kang, S. Han and J.-C. Lee, *J. Mater. Chem.*, 2012, **22**, 8654.

69 D. Sharon, P. Bennington, M. Dolejsi, M. A. Webb, B. X. Dong, J. J. de Pablo, P. F. Nealey and S. N. Patel, *ACS Nano*, 2020, acsnano.0c03713.

70 B. X. Dong, P. Bennington, Y. Kambe, D. Sharon, M. Dolejsi, J. Strzalka, V. F. Burnett, P. F. Nealey and S. N. Patel, *Mol. Syst. Des. Eng.*, 2019, **4**, 597–608.

71 M. G. Martin and J. I. Siepmann, *J. Phys. Chem. B*, 1998, **102**, 2569–2577.

72 J. M. Stubbs, J. J. Potoff and J. I. Siepmann, *J. Phys. Chem. B*, 2004, **108**, 17596–17605.

73 K. A. Maerzke, N. E. Schultz, R. B. Ross and J. I. Siepmann, *J. Phys. Chem. B*, 2009, **113**, 6415–6425.

74 C. D. Wick and D. N. Theodorou, 2004, 7026–7033.

75 N. C. Lopes and B. Pascal, *J. Chem. Phys. B*, 2004, **108**, 16893–16898.

76 W. M. Brown, A. Kohlmeyer, S. J. Plimpton and A. N. Tharrington, *Comput. Phys. Commun.*, 2012, **183**, 449–459.

77 S. Plimpton, *J. Comput. Phys.*, 1995, **117**, 1–19.